Weather-dependent passive thermography and thermal simulation of in-service wind turbine blades

Weather-dependent passive thermography and thermal simulation of in-service wind turbine blades

Somsubhro Chaudhuri[1], **Michael Stamm**[1], **Rainer Krankenhagen**[1]
[1]Bundesanstalt für Materialforschung und -prüfung, Germany
E-mail: somsubhro.chaudhuri@bam.de

Abstract. To cope with the increase in the manufacturing and operation of wind turbines, wind farm operators need inspection tools that are able to provide reliable information while keeping the downtime low. Current inspection techniques require the wind turbine to be stopped. This work presents the current progress in the project EvalTherm, in which passive thermography is evaluated as a possible non-destructive inspection tool for operational wind turbine blades (WTBs). A methodology to obtain thermal images of rotating WTBs has been established in this project. However, the quality of the results is heavily dependent on various aspects such as weather conditions, information on the inspected WTB, damage history, etc. In this work, a section of a used WTB is simulated using finite-element modelling (FEM) as well as experimentally tested for evaluating the accuracy of the model. Such a model will provide insight into the potential thermal response of a certain structure (with specific material properties) in given weather (boundary) conditions. The model is able to provide satisfactory predictions of the temporal thermal response of the structure, as well as indicate what thermal contrast(s) transients result from artificial defects introduced in the structure.

1. Introduction

To achieve the carbon neutrality goals set at COP26, the number of wind turbines in operation and construction is exponentially increasing [1] (currently at 837 GW worldwide in 2021 [1]). This increases the effort of maintaining such infrastructure for the operators of wind turbine farms, both on-shore and off-shore [2]. This is further exacerbated by the complex structure of wind turbine blades (WTBs) that makes inspection and evaluation of findings a challenge. WTBs are multi-material (glass/carbon fibre reinforced polymer G/CFRP, balsa wood or PVC foam, glue, etc.) structures based on specific, proprietary designs [1, 3]. Approximately 65% of all failure incidents related to wind turbines are related with WTBs [4, 5]. To avoid premature WTB failure, a range of inspection techniques have been developed and currently used in operation [3, 4, 6, 7]. Infrared thermography (IRT) is one of them [8, 9, 10, 11]. The work presented here is part of an ongoing multi-partner project titled "EvalTherm": the evaluation of passive thermography as a non-destructive inspection tool of WTBs in operation [12]. This paper specifically discusses the aspect of performing ground-based passive thermography on WTBs and the corresponding issues. Finite-element (FE) based simulations are performed using COMSOL Multiphysics® to simulate the thermal response of a WTB. This enables introducing known defects in the FE model and simulating their thermal response. Field measurements are compared with the simulation results to possibly link defect signatures observed in the field with the simulation results of artificial defects. Apart from passive thermography, other

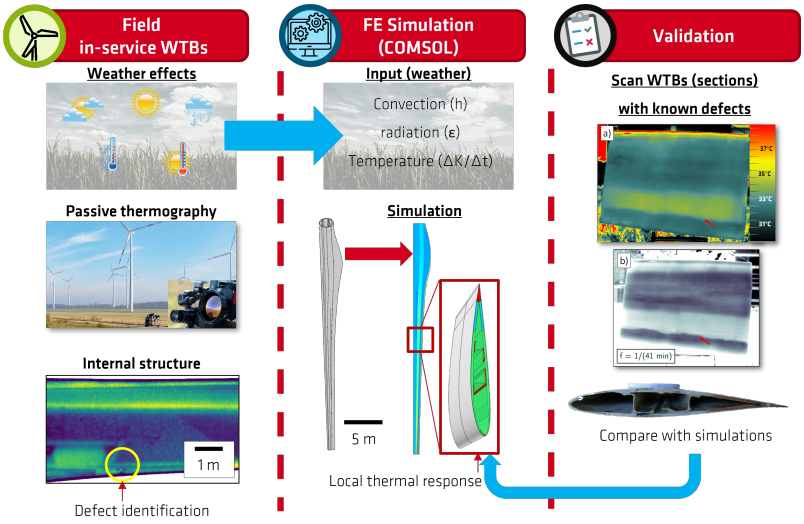

Figure 1. Schematic of the EvalTherm workflow.

partners of the EvalTherm project will be working on comparing the results obtained from passive thermography with active thermography results and on additional aspects crucial for bringing this technology into service. However, this is beyond the scope of this paper.

2. Approach

To understand and simulate the thermal behaviour of a WTB in operation, not only the external conditions but also the entire internal structure of the WTB must be known. Since the expected, and observed, defect related thermal contrasts in relation to usual surface temperature distributions on WTBs are low (<1 K) [10, 13, 14, 15]. Even minor details of the inner structure can have a large impact on surface temperatures.

Recently, a lab experiment was performed on a WTB section with the objective of linking experimental measurements and FE simulations using COMSOL Multiphysics [16]. It turned out that even a difference of 0.5 cm for a shell thickness of 2 cm strongly influences the thermal detectability of inner features like beam bonding (not reported so far). Unfortunately, such detailed information is usually not available for the wind turbine operator or the inspection companies. In order to perform useful thermal simulations focus is given on cut sections of old blades where the structural details are known from the cross-section views [16].

In addition, a scalable FEM model of an entire rotor blade was developed based on a typical structure. The goal is a general blade model which can be fitted to a specific design by a range of geometrical parameters and shape factors. It will be described in more detail in a later report. Here, we will focus on the cut part of a WTB which is sufficient to investigate the spatial and temporal evolution of thermal contrasts on the outer surface, at least in a first approximation. Later, if a suited wind turbine with sufficient information about the inner blade structure is found, the FEM simulations will be extended to the qualitative simulations of thermal contacts.

The running activities of the project are summarised in the following scheme (Figure 1). Field inspection of in-service WTBs is performed using ground-based passive thermography. In parallel, a simulation of the WTB structure with input parameters and boundary conditions based on measurements performed during corresponding field measurements is developed to predict the thermal response of the WTB. Comparing these simulations with real data acquired with passive and active thermography allows the validation of simulated thermal responses, and thus provide a method of predicting possible thermal contrasts in a range of weather conditions.

Figure 2. A schematic of the IRT camera setup.

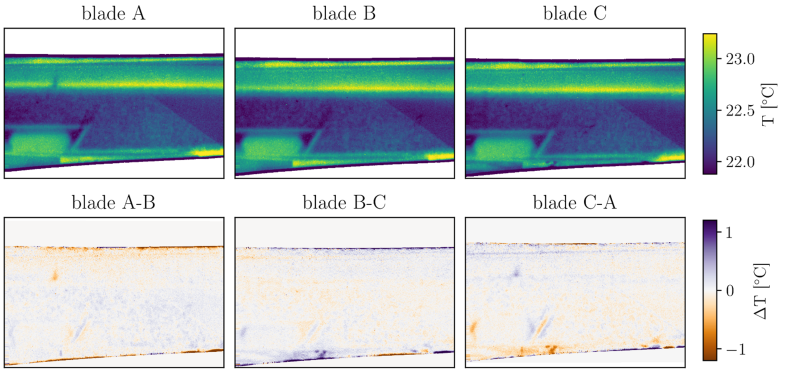

Figure 3. TOP: Surface temperature of 3.6 m long section of a WTB; BOTTOM: temperature differences between the different blades. Taken from [16].

The field inspection process is briefly described in section 3 to provide the overarching concept being developed in this project, lab measurements are described in section 4, and initial FE model validation results are shown in section 5. Section 6 summarises the conclusions from this work and outlines the next steps in the ongoing EvalTherm project.

3. Field inspection of in-service WTBs

Field inspection of in-service WTBs is performed using ground-based passive thermography (Figure 2). As an example, an in-service wind turbine with 35 m long WTBs was scanned during the month of August in central Germany. The wind turbine was in regular operation and not stopped for the inspection procedure. The IRT camera used is an ImageIR 8800 long-wave IR camera from Infratec GmbH. Camera specifications are provided in Table 1. The table also includes specifications when the IR camera is used for lab measurements (described in section 4.2.1). The camera is set up on a pan-tilt unit (PTU) which allows for programmable camera panning to automatically capturing the rotating WTBs. With such a semi-automatic measurement setup, the data acquisition is fast and takes about three minutes of scanning time (excluding approximately 5-10 minutes of moving the setup to the other side of the WTBs) for the suction and pressure side respectively.

In the shown scenario (Figure 3), it was attempted to capture internal structure of the blade while the heat source, the Sun, is shining on the opposite side of the scanned blade. Special attention is given to identifying optimum weather conditions for obtaining the best possible thermal contrast. Thermal images of 3.6 m long sections of the WTB are taken from the ground at a distance to the tower of 90 m and are shown in Figure 3. Here, some details of the internal structure of the WTB are visible. Using a specifically developed and patented post-processing workflow where the temperature differences of the three blades are taken [10, 16], anomalies in the structure of the blade can be identified and marked.

4. WTB section lab measurements

The purpose of performing lab measurements is to be able to limit the number of influencing factors involved in the field, in order to better understand the effect of each individual factor, and subsequently benchmark an FE model. It is also worth mentioning that it is challenging to obtain accurate WTB design documents from manufacturers due to commercial reasons like intellectual properties on the part of manufacturers. Thus, lab measurements of used WTBs become a

Table 1. Camera and measurement specifications for lab measurements and field inspection..

Parameter	Lab experiment	Field measurement
Detector	Cooled Hg1-xCdxTe	
Wavelength	8-9.2 µm	
Detector resolution	640 x 512 pixels, pixel pitch: 16 µm	
Integration time	140 µs	
Calibrated temperature range	0-60°C	
NETD	47 mK	
Assumed emissivity	1	
Objective focal length	25 mm	200 mm
Distance to object	3.05 m	90 m
Field of view	1.25 x 0 .99 m	4.6 x 3.7 m

feasible alternative. Stamm and Krankenhagen [16] have performed these measurements for a specific sample extracted from a used WTB, where half of the width of the blade was removed for simplifying the problem and also for observing the inner section of the WTB. In this work, a full section of a used WTB is tested. The dimensions of the specimen and a cross-sectional image are shown in Figure 4. The section is 1 m long and has a maximum chord length of 765 mm.

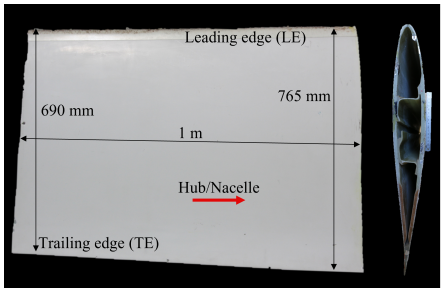

Figure 4. Schematic of the rotor blade section showing the dimensions and the cross-section.

4.1. FE model

COMSOL Multiphysics software package version 6.1 with Heat Transfer module was used for FE modelling. For defining the geometry of the WTB section as accurately as possible, detailed measurements of the cross-section shown in Figure 4 were taken. This included the different materials that form the blade such as glass fibre reinforced plastic (GFRP), sandwich foam, resin or glue, and the skin, shown in Figure 5. Thermal properties of the different materials have been taken from [16] and are provided in Table 2. Experimental validation of these parameters is planned in next steps of the project. It is important to note that the GFRP is assumed to behave like an isotropic material when it comes to macroscopic thermal effects which are of interest in this study. Also, the skin is given the same material properties as the GFRP for the sake of simplicity. The influence of radiant cooling (with an emissivity of 0.95 as an influence of the coating on the skin) was included on the irradiated surface (the skin).

Different types of simulations have been performed for the WTB section, including the simulation of thermal measurements performed in the lab as well as measurements performed outside. They are explained in detail in section 4.2. The FE mesh has been generated within COMSOL. For the sake of brevity, the mesh construction is not discussed in this paper, but will be presented with a mesh study in a following report.

Table 2. Thermal properties.

Material	Thermal conductivity k $Wm^{-1}K^{-1}$	Mass density ρ Kgm^{-3}	Heat capacity C_p $Jkg^{-1}K^{-1}$
GFRP	0.35	1800	1000
Foam	0.03	35	1300
Glue	0.28	1300	1280

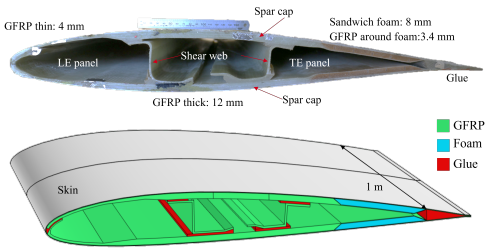

Figure 5. Schematic of the cross-section showing the different materials and thickness distribution.

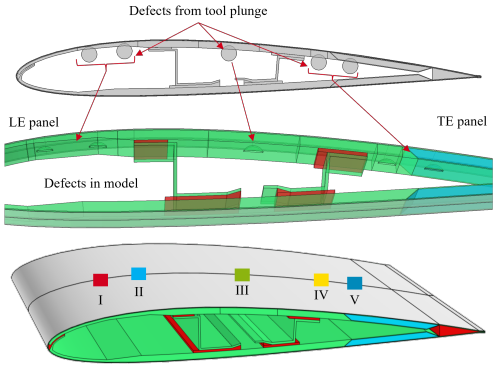

Figure 6. Schematic showing the introduction of defects into the COMSOL model.

As this study is an evaluation trial of the methodology of studying the effect of defects on the thermal response of the WTB section both experimentally and in simulations, defects have been machined in the WTB section using a Dremel multi-purpose tool. Essentially, semi-elliptical troughs were milled on inner surfaces as artificial defects . It is understood that this is not strictly representative of a real defect but rather a simplified loss of material thickness. However, in the next steps of this project, WTB sections with known and documented realistic defects will be scanned and modelled using the developed methodology. This is beyond the scope of this paper. In the COMSOL model, the defects are generated using a similar method where the intersecting elements of the WTB with the milling tool are removed to create the groove-like defect(s), see Figure 6. The defects are numbered I-V. Defects I and III are used as examples in section 5. The dimensions are given in Table 3. This technique (along with the correct choice of mesh elements - tetrahedral in this case) allows for complex defect configurations such as defect V in the TE panel going through both the foam and the inner GFRP skin. Additionally, such a model allows a relatively straightforward comparison between the thermal response of the WTB section without and with defect(s).

The following boundary conditions for the heat transfer module in COMSOL were used:

(1) Radiation: the value of radiation was obtained using a Hukseflux Pyranometer model SR-03. It was obtained in Wm^{-2}.

(2) Initial temperature: It can be assumed, that the measurements are performed when the specimen is in a thermal steady state, hence the surface temperature of the specimen is equal to the inner temperature of the specimen. This is generally equal to the air temperature in the lab where the specimen was stored. In the case of outdoor measurements, the specimen was stored outside overnight, and the initial temperature was taken as the temperature of the surface of the specimen at the time of thermal scanning.

(3) Ambient temperature: for lab measurements, this was set to the air temperature regulated by the air conditioning system (21.5°C). For external measurements, this was measured.

Table 3. Defect characteristics.

Defect #	Depth [mm]	Length [mm]	Width [mm]
I	4	15-18	8
II	4	15-18	8
III	6	40-45	8
IV	5	30-35	8
V	5	30-35	8

4.2. Experimental setup
To compare with the results obtained from the COMSOL model, the WTB section is setup in lab conditions as well as outside. Both are described briefly below.

4.2.1. Lab measurement The WTB section is setup in lab conditions with controlled air temperature. The heat source is a SuperBeam 1200 rated 1200 W, which is used as a (lab) substitute for the Sun. The primary disadvantage of this setup is that it is not possible to replicate the homogenous heating by the Sun with an artificial heat source. Thus, each defect location was heated and scanned separately and compared with the FE simulation in which a homogenous heating across the surface of the specimen (subject to the curvature of the surface) is considered. A basic schematic is shown in Figure 7. A pyranometer was used to measure the intensity of the heating provided by the SuperBeam in Wm^{-2}, such that the values can be used as input for the COMSOL model.

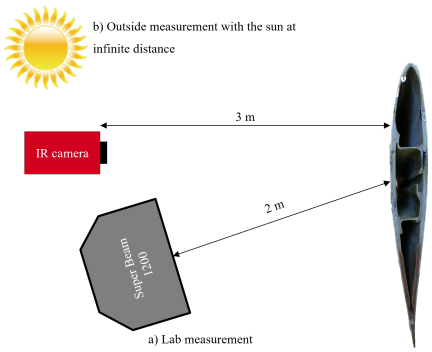

Figure 7. Basic schematic of the IR camera, specimen, and heat source setup; a) lab measurement with SuperBeam 1200; b) outside measurement with the sun..

5. Results and discussion
In total, three different kinds of experiments were performed. Details are provided in Table 4. All the three tests have the same specimen and defects. The defects are detailed in Table 3. It is important to highlight that it was expected and confirmed, that the boundary conditions strongly influence the detectability of defects with different characteristics. The experimental results are compared with the simulations. For the sake of brevity, results of Tests #1 and #3 are presented here. Test #1 represents a case of active thermography where the user actively

Table 4. Table of the three different types of tests performed.

Test ID	Test location	Ambient temperature at beginning of test	Specimen temperature at beginning of test	Source of radiation
Test #1	Lab	21.6°C	23.7°C	SuperBeam
Test #2	Lab	21.6°C	5°C	None (heating from ambient air)
Test #3	Outside	1°C (gradually increased with time)	3°C	Sun

controls the heat source (SuperBeam). Test #3 is passive thermography with the Sun being the source of heating.

5.1. Test #1

For Test #1, the specimen was stored in the lab and heated for a specific period with the SuperBeam. As homogenous heating on the entire surface of the WTB is not possible in this arrangement, results shown here focus on defect I (from Figure 5) located in the leading edge and thinnest GFRP section. For the first 60 seconds of the measurement, no heating is turned on. Henceforth, 10 minutes of heating is provided by turning on the SuperBeam to full rated power. From the Pyranometer, it could be seen that the SuperBeam at a distance of 2 m to specimen provided an irradiation of 1200-1300 Wm^{-2}. Using optical spectrometry, preliminary reflection measurements of the coating of similar WTB blades were performed. Results showed that such WTB coatings offer an average of 50% reflection in the long wave infrared spectrum of the sun. This reflection was accounted for in the boundary conditions used in the COMSOL model for Test #1.

Figure 8 presents a thermogram of the specimen taken once the SuperBeam has been turned off after 10 min heating but remained for approximately 5 minutes in front of the specimen. The turning off of the SuperBeam is indicated as "End of heating" and is highlighted in Figure 9 and Figure 10. It is shown as a region and not a singular point as the heat source is manually reduced in intensity from 100% to 0%, thus it is not instantaneous. Due to the reduced thickness of GFRP above the defects as compared to the surrounding bulk material, a thermal contrast appeared after a certain period of heating (100+ seconds), and the defect was visible in the IR data without additional image post-processing. Figure 9 presents the temporal temperature distribution obtained from lab measurements as well as from the COMSOL simulation at Defect I. Even though the absolute temperature is not the same, the simulation was satisfactorily able to predict the shape of the temperature transient at the specimen surface. The difference in peak temperature is likely to be attributed to inaccuracies in the material properties (not just of the GFRP, but also of surrounding material) and boundary conditions (in the room). Another interesting location is the anomalous heating in the region between 750-900 seconds of scanning. This is attributed to residual infrared radiation from the SuperBeam even after it was turned off (because of the hot halogen lamp). After the heating, the face of the SuperBeam heat source was turned away from the specimen. It was covered with black fabric to reduce the added reflection on the WTB section at approximately 900 seconds of the recording. This highlights the strong influence of a range of boundary conditions (other than the obvious) on the measurements, confirming what previous authors have also acknowledged in such experiments.

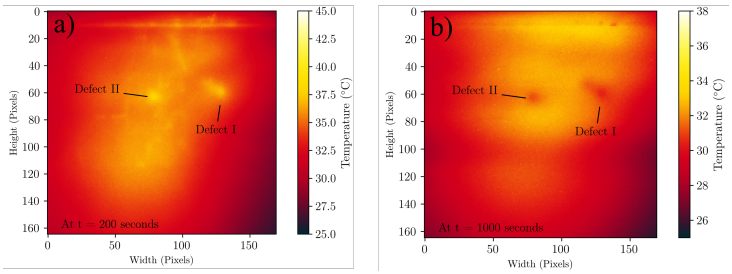

Figure 8. Test #1: Section of WTB which contains defects. a) Thermogram is taken at time of maximum thermal contrast (ΔT, Figure 10)
; b) Thermogram is taken approximately 5 minutes after the heat source is turned off.

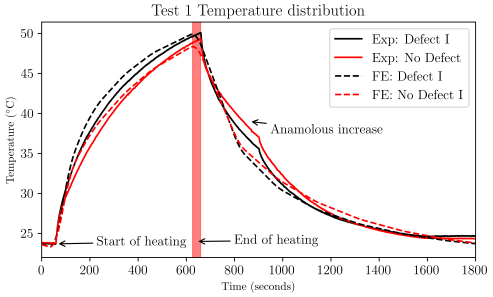

Figure 9. Temperature distribution from experimental data and simulation data of Test #1.

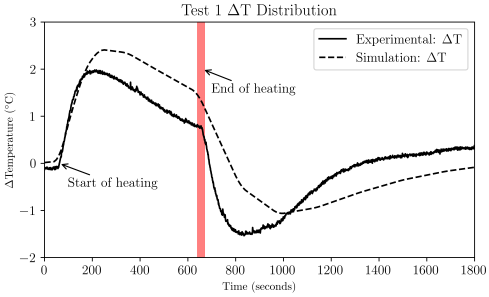

Figure 10. Distribution of the temperature difference in the presence and absence of a defect (ΔT) of Test #1.

Figure 10 comprises the same data sets but shows the difference between a defect region and a sound region. This thermal contrast (ΔT) is the actual signal in thermographic defect detection. For the experiment, the results showed that maximum ΔT was achieved at approximately 200 seconds of the measurement, which highlights that ideally the test could be stopped after this exposure. Figure 8a) shows the thermogram at this instant. If the defect related ΔT is higher than the thermal resolution of the camera (see Table 1) and other external noise like reflections or inhomogeneous convection, it should be possible for the defect to be detected without extensive post-processing. Thermograms in Figure 8$a-b$ have not been post-processed (apart from defining a certain temperature range for the colour scheme) and show the defects to be distinguishable. Additionally, Figure 10 also shows the simulated ΔT for the same experimental conditions. It can be observed that the FE simulation over-predicts the ΔT, but provides a reasonable estimation of the contrast transient, especially in terms of a peak early in the heating process. The authors assume an increased lateral heat conductivity as the reason for this deviation. The anisotropy of the thermal conductivity in GFRP is known and was reported earlier in [14]. The lateral diffusion of a hot spot reduces its maximum intensity and thus the ΔT. This effect was not regarded in the simulation leading to an enhanced simulated ΔT. Such a combination of experimentally measured thermal properties followed by thermal simulation is not readily available in the literature and it is planned in the future work of the EvalTherm project.

5.2. Test #3

For Test #3, the specimen was kept outside overnight. Before scanning, the inside of the specimen was at 1 °C. To protect the specimen from the Sun, the specimen was covered during the

camera setup. However, the outer layer reached (not intended for the experiment) approximately 5 °C (due to the Sun's radiation) before the measurements could begin. This was accounted for in the COMSOL simulation. Figure 11 is a thermogram of the specimen with defects III and I visible. Defect III is in the thickest section (12 mm) of the GFRP, and this defect was not visible in the unprocessed thermogram in Tests #1 and #2. This is attributed to the relatively stronger thermal flux generated due to the homogenous irradiation of the Sun (in contrast to the SuperBeam) on the surface of the WTB and the relatively colder air temperature of approximately 1 °C (see Table 4). This also enables the internal structure of the WTB to be visible without any additional post-processing. However, post-processing can help mitigate (to a certain extent) effects of strong reflections as well as noise in the image due to dead camera pixels. Irregularities in the internal structure can be visualized as well, but this is beyond the scope of this paper.

Figure 12 presents the temporal temperature distribution obtained experimentally at the location of defect III and a location in the same material without any defect. These are compared with the simulation data. As expected, the temperature measured at the surface increases with time due to the radiation from the Sun. The simulation results are satisfactorily able to predict trends in the thermal response of the WTB section. The temperature profile is different from Test #1 (Figure 9) as the recording is taken for a period of 30 minutes with the specimen exposed to the Sun (in Test #1 the source of heat is turned off after 10 minutes). The simulation results for Test #3 have a deviation in the results, specifically the rate of temperature increase in the first half of the test. It is important to highlight the incremental number of boundary conditions that arise to outside measurements, and only some can be incorporated in the simulations. Such factors are namely air temperature, wind speed, convection (free or forced), irradiation from the Sun, reflection from buildings, etc. The difference between the experiment and simulation can thus be attributed to this. As it is not always possible to measure every parameter, a parametric study would be a possible way of understanding which values should be prioritized (in addition to the parameters already measured such as air temperature and irradiation).

Figure 13 shows the resulting thermal contrast (ΔT) due to the presence of defect III (black). The ΔT is approximately 0.3 K which, from experience, is close to what is the detection limit in the field (see Figure 3). This indicates the possibility for defect detection without sophisticated image post processing (Figure 11). In the simulation, ΔT is constant during the duration of the experiment for defect III, which is not seen in the ΔT observed for defect I (blue in Figure 13). The authors attribute this to the difference in material thickness at the defect location. The thicker the material, the longer it would take for a homogenous temperature distribution to occur (thus loss of ΔT). If the experiment had been allowed to run longer than 30 minutes, a decline in ΔT could be expected for Defect III (such a trend is seen in the simulation). This behaviour is seen in Defect I, where with time, the contrast is slowly lost (the GFRP section around Defect I is 3 times thinner than Defect III). The simulations provide a reliable estimate of the ΔT transient. For Defect III, the simulation predicts an eventual reduction in ΔT, which is not seen in the experiments. This could be attributed to the anisotropic behaviour of the GFRP material, specifically the anisotropy in thermal conductivity. Due to the directional construction of GFRP, it is plausible that with use (the WTB section tested is a used section with an unknown load history) the thermal conductivity has also altered. This has not been accounted for in the simulation.

6. Conclusions and Future Work

The primary aim of this work was to evaluate the accuracy of the FE model and possibly extract information regarding thermal contrast resulting due to defects. The FE models can provide indicative trends of the thermal response of the tested WTB section, provided the boundary conditions are recorded as accurately as possible. Material properties play a critical role and

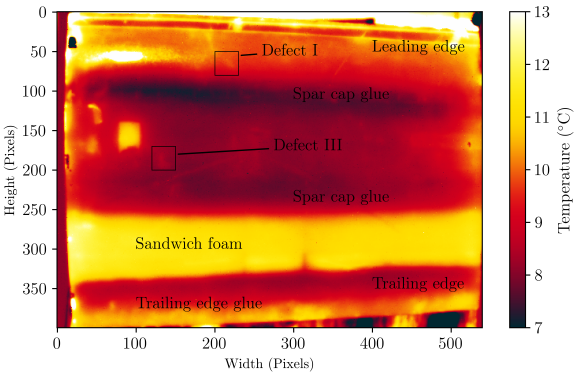

Figure 11. Test #3: Thermogram of the specimen with defect III visible.

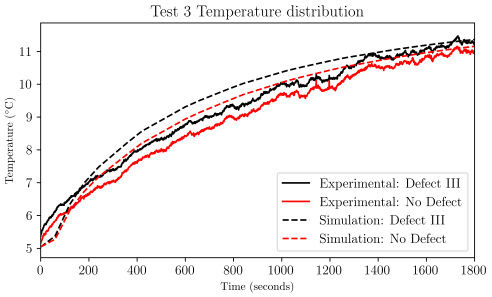

Figure 12. Temperature distribution from experimental data and simulation data of Test #3.

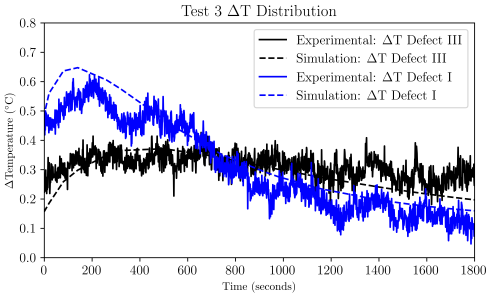

Figure 13. Distribution of the temperature difference in the presence and absence of a defect (ΔT) of Test #3.

should be measured for individual materials to improve the accuracy of the FE model. The thermal contrasts obtained are sufficient to visualize the defects without any additional image post-processing. However, post-processing could be beneficial for removing noise and segmenting the internal structure in the images.

To further improve upon this work, the following future work is planned:

- The defects produced in this work are not representative of real defects. It is planned in this project to procure specimens that contain known defects which better represent reality. Also, it is planned to include defect data from other NDT techniques such as X-ray computed tomography.
- Experimental evaluation of thermal material properties which also includes the measurement of reflectance of the coating used on WTBs.
- The long-term aim of the project is to extend the FE modelling to full-scale WTBs, in line with the already implemented methodology of field inspection of in-service WTBs and include the influence of weather conditions.

Acknowledgments
The results presented were obtained within the EvalTherm project and the authors would like to thank the project partners for their cooperation. Special thanks to Julien Lecompagnon for his guidance in data processing and formatting.

References

[1] Global Wind Energy Council (GWEC). Global wind report 2022. Report, GWEC, 2022.
[2] Wenxian Yang, Peter J. Tavner, Christopher J. Crabtree, Y. Feng, and Y. Qiu. Wind turbine condition monitoring: technical and commercial challenges. *Wind Energy*, 17(5):673–693, 2014.
[3] Y. Du, S. Zhou, X. Jing, Y. Peng, H. Wu, and N. Kwok. Damage detection techniques for wind turbine blades: A review. *Mechanical Systems and Signal Processing*, 141, 2020.
[4] M. Civera and C. Surace. Non-destructive techniques for the condition and structural health monitoring of wind turbines: A literature review of the last 20 years. *Sensors*, 22(4), 2022. Export Date: 30 September 2022; Cited By: 6.
[5] Sander R. Brouwer, Saad H. S. Al-Jibouri, Ibsen Chivatá Cárdenas, and Johannes I. M. Halman. Towards analysing risks to public safety from wind turbines. *Reliability Engineering & System Safety*, 180:77–87, 2018.
[6] I. Amenabar, A. Mendikute, A. López-Arraiza, M. Lizaranzu, and J. Aurrekoetxea. Comparison and analysis of non-destructive testing techniques suitable for delamination inspection in wind turbine blades. *Composites Part B: Engineering*, 42(5):1298–1305, 2011.
[7] Renaldas Raišutis, Elena Jasiuniene, Reimondas Sliteris, and A. Vladišauskas. The review of non-destructive testing techniques suitable for inspection of the wind turbine blades. *Ultrasound*, 63, 2008.
[8] D. Traphan, I. Herráez, P. Meinlschmidt, F. Schlüter, J. Peinke, and G. Gülker. Remote surface damage detection on rotor blades of operating wind turbines by means of infrared thermography. *Wind Energ. Sci.*, 3(2):639–650, 2018. WES.
[9] H. Sanati, D. Wood, and Q. Sun. Condition monitoring of wind turbine blades using active and passive thermography. *Applied Sciences (Switzerland)*, 8(10), 2018. Export Date: 30 September 2022; Cited By: 22.
[10] M. Doroshtnasir, T. Worzewski, R. Krankenhagen, and M. Röllig. On-site inspection of potential defects in wind turbine rotor blades with thermography. *Wind Energy*, 19(8):1407–1422, 2016.
[11] C. Galleguillos, A. Zorrilla, A. Jimenez, L. Diaz, Á L. Montiano, M. Barroso, A. Viguria, and F. Lasagni. Thermographic non-destructive inspection of wind turbine blades using unmanned aerial systems. *Plastics, Rubber and Composites*, 44(3):98–103, 2015. Export Date: 30 September 2022; Cited By: 33.
[12] BAM. Project webpage: Evaltherm - passive thermography for the detection of rotor blade damage on wind turbines, 2020.
[13] T. Worzewski, R. Krankenhagen, M. Doroshtnasir, M. Röllig, H. Steinfurth, and C. Maierhofer. Forschung zur thermografischen zustandsinspektion von offshore rotorblättern. *Wind-Kraft-Journal*, (February), 2014.
[14] Tamara Worzewski, Rainer Krankenhagen, Manoucher Doroshtnasir, Mathias Röllig, Christiane Maierhofer, and Henrik Steinfurth. Thermographic inspection of a wind turbine rotor blade segment utilizing natural conditions as excitation source, part i: Solar excitation for detecting deep structures in gfrp. *Infrared Physics & Technology*, 76:756–766, 2016.
[15] Tamara Worzewski, Rainer Krankenhagen, and Manoucher Doroshtnasir. Thermographic inspection of wind turbine rotor blade segment utilizing natural conditions as excitation source, part ii: The effect of climatic conditions on thermographic inspections – a long term outdoor experiment. *Infrared Physics & Technology*, 76, 2016.
[16] M. Stamm and R. Krankenhagen. Weather-dependent passive thermography of unheated wind turbine blades. In *Proc.SPIE*, volume 12109, page 121090E, 2022.